Metal-Supported Solid Oxide Fuel Cells Operated in Direct-Flame Configuration

Michael C. Tucker* and Andrew S. Ying

Energy Conversion Group, Energy Technologies Area

Lawrence Berkeley National Laboratory

1 Cyclotron Rd

Berkeley, CA 94720 USA

Abstract

Metal-supported solid oxide fuel cells (MS-SOFC) with infiltrated catalysts on both anode and cathode side are operated in direct-flame configuration, with a propane flame impinging on the anode. Placing thermal insulation on the cathode dramatically increases cell temperature and performance. The optimum burner-to-cell gap height is a strong function of flame conditions. Cell performance at the optimum gap is determined within the region of stable non-coking conditions, with equivalence ratio from 1 to 1.9 and flow velocity from 100 to 300 cm s^{-1}. In this region, performance is most strongly correlated to flow velocity and open circuit voltage. The highest peak power density achieved is 633 mW cm^{-2} at 833°C, for equivalence ratio of 1.8 and flow velocity of 300 cm s^{-1}. The cell starts to produce power within 10 s of being placed in the flame, and displays stable performance over 10 extremely rapid thermal cycles. The cell provides stable performance for >20 h of semi-continuous operation.

Metal-supported SOFC; direct flame sofc; thermal cycling

*mctucker@lbl.gov

Phone 1-510-486-5304

Fax 1-510-486-4260

LBNL; 1 Cyclotron Rd; MS 70-108B; Berkeley CA 94720; USA

1. Introduction

Solid oxide fuel cells (SOFCs) operate at elevated temperature, typically 600-900°C, and require electrochemically-active fuel such as H_2 or CO to produce power. An extremely simple way to fulfill these requirements is to place the anode of the SOFC in contact with a flame, which provides the necessary heat and contains H_2 and CO within the primary combustion zone. This "direct-flame" setup yields relatively low performance and very low fuel-to-power efficiency, but has been studied extensively in the literature due to the simplicity and appeal of the system; no costly balance of plant is required to produce power [1–26]. Applications including an integrated multi-cell microtubular stack [13,23], and small portable power system providing power as a byproduct of cooking have been demonstrated [20], a tri-generation system for power, heating, and cooling has been analyzed [27], and deployment can be envisioned anywhere that flames are available, including industrial heating, residential water heating, and well-head gas flares. Low electrical efficiency is expected for such scenarios, as much of the fuel is combusted to produce heat, but the direct flame configuration can provide electricity where none is otherwise available.

Direct-flame SOFCs have been operated with a variety of gaseous, liquid, and solid fuels, including methane [2], propane [6], butane [4], ethylene [5], ethanol [15], methanol [8], parrafin [4], and wood [4]. Very high power density is reported for methane and propane at high equivalence ratios [18,19], although soot and coke formation is a concern at this operating condition. At lower equivalence ratios, where stable operation with no carbon deposition on the cell is expected, moderate power density in the range 100 to 500 mW cm^{-2} is typical (see Figure 6b). Coking is also influenced by fuel type, for example a cell operated in direct methanol flame showed stable performance over 30 h, whereas a similar cell operated with ethanol flame failed very quickly due to carbon deposition on the anode [8]. Direct-flame SOFCs have been operated with a wide variety of burner configurations, including jet burner tube which provides a simple setup and stable flame [19], micro-jet flame [7], multi-element diffusion flame burner [16], and

flat flame burner [28] which provides very uniform temperature and concentration distributions across the cell area.

Key flame parameters reported in the literature include the burner-to-cell gap height, equivalence ratio (stoichiometric ratio of fuel to oxygen in the air/fuel mixture), and flow velocity (the linear speed of the fuel-air gas mix exiting the burner before combustion). Key SOFC metrics include the temperature, polarization behavior or power density, and open circuit voltage (OCV). OCV in the range 750 to 950 mV is typical, and OCV near the theoretical maximum can be achieved [12,28], suggesting that the effects of mixing of fuel and air at the unsealed edge of the cell can be minimized. Note that SOFCs operating pure hydrogen vs. air display OCV near 1.1 V; the lower OCV for direct-flame configuration is a consequence of the relatively lower concentration of electrochemically-active fuel species (H_2 and CO) and higher oxygen partial pressure (CO_2, H_2O) present in the flame [6,28]. The concentration of all species varies spatially within the flame, so optimal placement of the cell within the flame can be important for maximizing performance.

Nearly all of the direct-flame literature to date has utilized anode-supported SOFCs (ASCs). In this work, we characterize the performance of a metal-supported SOFC (MS-SOFC) in direct-flame configuration, which to the best of our knowledge is the first such study. The MS-SOFC architecture, shown in Figure 1 is symmetric, with porous stainless steel supports and porous YSZ electrode layers bonded to both sides of the YSZ electrolyte. Nano-scale catalysts are introduced into both electrodes by infiltration, as described in recent work [29]. MS-SOFCs are particularly well suited to direct-flame operation due to their tolerance to thermal cycling and anode re-oxidation, and provide additional benefits including low materials cost, mechanical ruggedness, and in some cases high power density [30]. The performance of the MS-SOFC is systematically mapped over a wide range of flame operation parameters, including burner-to-cell gap height, equivalence ratio, and flow velocity. A tubular burner is used for simplicity, and a MS-SOFC with small circular active area is used to match the flame shape and minimize

temperature and fuel concentration variations across the active cell area as shown in Figure 1d. Propane is chosen as the fuel, due to its application throughout the world as a cooking fuel, and therefore its relevance to combined cooking-and-power devices.

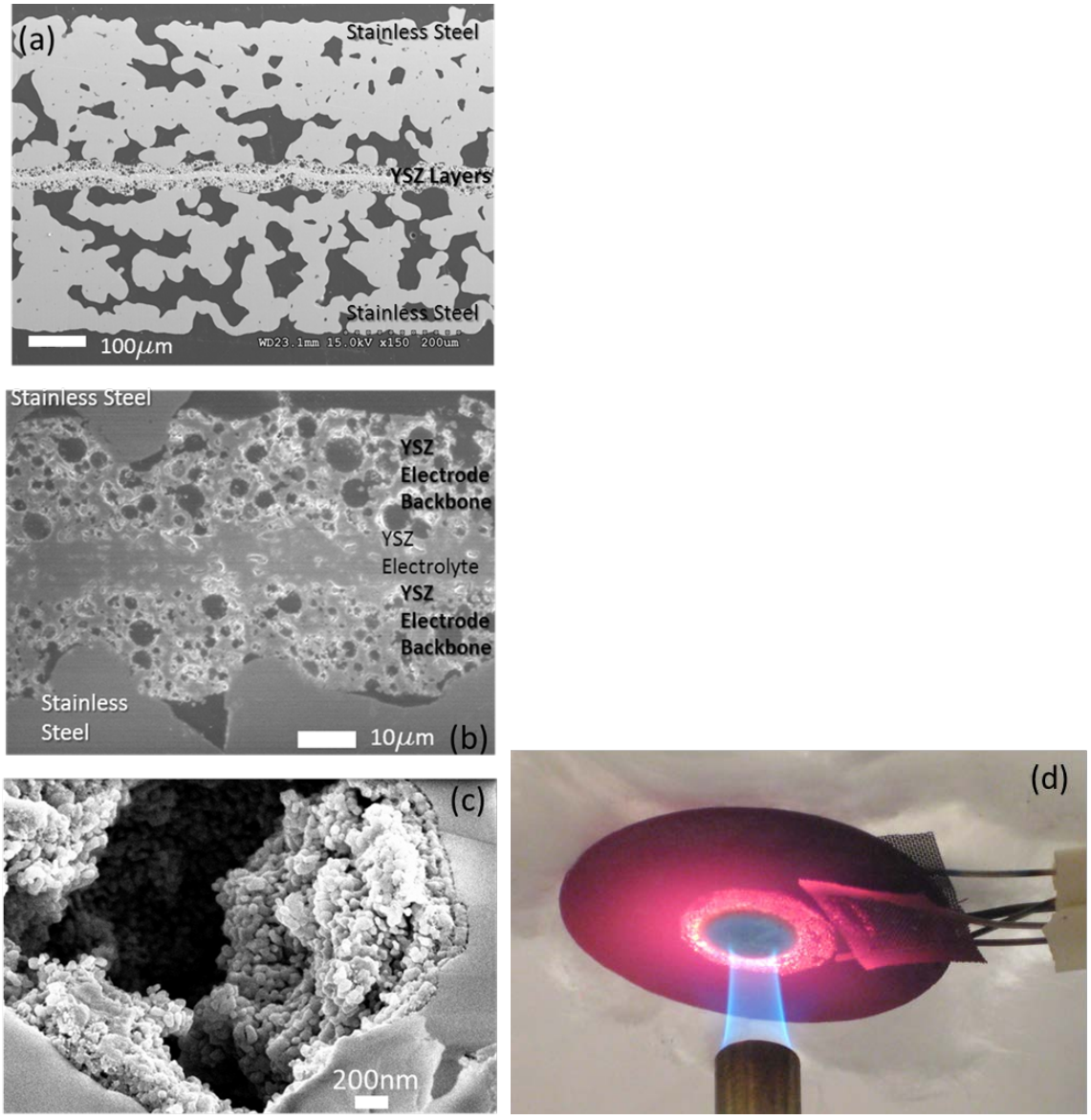

Figure 1. MS-SOFC and flame setup. SEM image of (a,b) polished cross section of MS-SOFC structure after sintering and before catalyst infiltration, and (c) cathode pore after infiltration of LSM nanoparticles. Reproduced from Reference [29] with the permission of the publisher. Approximate layer thicknesses are: metal support 250 μm, porous electrode 20 μm, and electrolyte 10 μm. (d) Picture of the anode side of

the cell with flame impinging on the 1 cm^2 active area in the center of the cell. Alumina wool insulation is loosely placed on the cathode (top) side of the cell.

2. Experimental Methods

Details of the cell fabrication and catalyst infiltration procedures are discussed elsewhere [29]. MS-SOFCs were fabricated from YSZ (8Y, Tosoh) and stainless steel (P434L alloy, water atomized, Ametek Specialty Metal Products) layers prepared by tape-casting. Individual tapes were laminated together to create the green cell structure. Cells were cut from the layered tape with a laser cutter (H-series, Full Spectrum Laser). Cells were debinded in air at 525ºC for 1 h, and then sintered in 2% hydrgen in argon at 1350ºC for 2 hours in a tube furnace. After sintering, cells were infiltrated by techniques described previously [31,32] with $La_{0.15}Sr_{0.85}MnO_{3-\delta}$ (LSM) on the cathode side and $Sm_{0.2}Ce_{0.8}O_{2-\delta}$ (SDC) mixed with Ni with a ceria:Ni volume ratio of 80:20 on the anode side. Each side was infiltrated 3 times to ensure appropriate catalyst loading. Vacuum was applied during each infiltration to assist evacuation of air and flooding of precursor into all pore space in the cell. The cathode was fully covered with catalyst, and the cell active area was defined by the anode, which was a 1cm^2 circle of catalyst centered in the cell area, and surrounded by bare cell area with no catalyst present.

Complete cells were suspended above the burner by NiCr wires that also acted as electrical contacts. Each side of the cell was contacted with two NiCr wires, attached with a small piece of NiCr mesh spot-welded to the wire and the cell. Platinum was not used, as it may catalyze gaseous reactions within the flame. The cell was held by a clamp and ring stand, which were mounted on a scissor jack to allow easy and accurate setting of the burner-to-cell gap. The cell was mounted horizontally over the burner, except as noted. The jet burner was a stainless steel tube, mounted vertically, and fed by air and propane mass flow controllers.

Air-fuel mixing occurred roughly 1 m upstream, to ensure adequate mixing before reaching the burner. A section of the burner tube was filled with 1 mm-diameter alumina beads to prevent flashback, develop uniform flow, and aid in air-fuel mixing. Anode reduction and performance of anode-supported cells (ASC) was assessed with commercial cells (MSRI) with Pt paste/Pt mesh current contacts on both electrodes. Open circuit voltage (OCV) and current-step I-V polarization were recorded with a multichannel potentiostat and current booster (Biologic). Throughout this work, reported temperatures are measured by a type K sheathed thermocouple mounted in the center of the cathode side of the cell, and held in place by spot-welded NiCr mesh.

Thermal cycling was achieved by placing the cell in a lit flame, and holding it there for at least 2 min to ensure complete heating. The cell was then removed from the flame and allowed to cool below 50°C, which took about 3.5 min. Temperature-time data were recorded with a data logger (Madgetech TC101A).

Continuous operation consisted of holding a cell at 0.45 V in a flame operating at 1.7 equivalence ratio and 250 cm s^{-1} flow velocity. Burner-to-cell gap was maintained at 2 cm. The cell was operated for several hours continuously, for several sessions. The flame was turned off between sessions, so as not to leave the flame unattended. The beginning of each session is visible in Figure 8 as a small excursion in current density.

3. Results and Discussion

3.1 Cell and flame system configuration

3.1.1 Flame operating space

A premixed flame of fuel and air was stabilized with a stainless steel jet burner. Various burner diameters were screened for flame stability and compatibility with the 1 cm^2 circular active area of the cell. Small burner inner diameter (0.3 cm) led to unstable flame blow-off over a wide range of the intended operating

space, as the flow velocity is higher for the same flowrate. Larger burner inner diameters (0.65 to 1.12 cm) resulted in lower cell temperature at fixed fuel-air flow conditions. The best performing burner inner diameter was found to be 0.48 cm (1/4" tube). The tubular burner produces a light blue inner flame cone where the fuel is partially combusted by the incoming air mixed with it. Directly outside the inner cone, the remaining fuel is consumed in the secondary combustion zone in contact with ambient air, which remains blue if complete combustion occurs. For this burner, temperature estimated with a small thermocouple in the inner flame cone was in the range 450 to 650°C, suggesting a mixture of pre-reaction and reaction zones, and the secondary combustion zone reached 1100°C. Note that these temperatures are indicative of the temperature the MS-SOFC will be exposed to in the different flames zones, and are not estimates of the adiabatic flame temperature, which typically exceeds 1400°C and is difficult to measure with a thermocouple [6,28,33,34]. An intermediate burner-to-cell gap is shown in Figure 1a, and both flame zones are in contact with the active area. The inner fuel-rich zone appears as a dark blue area in the center of the cell, surrounded by a bright orange ring of active anode area in contact with the hot secondary combustion zone and fully combusted hot gases. The large outer dark area of the cell is inactive (bare steel with no infiltrated catalysts). For this burner size and active area, the active area of the cell could easily be moved between complete coverage by the inner flame cone or removed to the secondary combustion and hot gas zone by adjusting the burner-to-cell gap. This has a large effect on cell temperature and fuel composition at the anode, as discussed below.

Independently controlling the air and fuel flowrates coming in to the burner allows access to a wide range of equivalence ratio and flow velocity. The observations of flame behavior are mapped out in Figure 2a. At equivalence ratio of 2 and above, a yellow or yellow-tipped flame occurred, indicating incomplete combustion and formation of soot. Placing the cell in such a flame quickly deposited soot on the anode. The desirable operation of a blue flame occurred for equivalence ratio roughly between 1 and 2. At the higher end of this range, coking on the anode is observed when the cell is placed in the flame. The limit for coke-free operation is indicated by the data points in the figure, obtained by placing a cell in the flame

and increasing the equivalence ration until carbon deposition was observed. The blue cone flame zone is extinguished at higher flow velocity by blow-off, in which the incoming gas speed exceeds the natural flame speed of the combustion front, and the flame lifts off the burner and extinguishes. At flow velocity below about 100 cm s^{-1}, the flame location was unstable, and the flame sometimes migrated inside the burner tube. Thus, the area of interest for fuel cell operation with this burner was defined as being above the blow-off limit, below the coking limit, and in the flow velocity range of 100 to 350 cm s^{-1}.

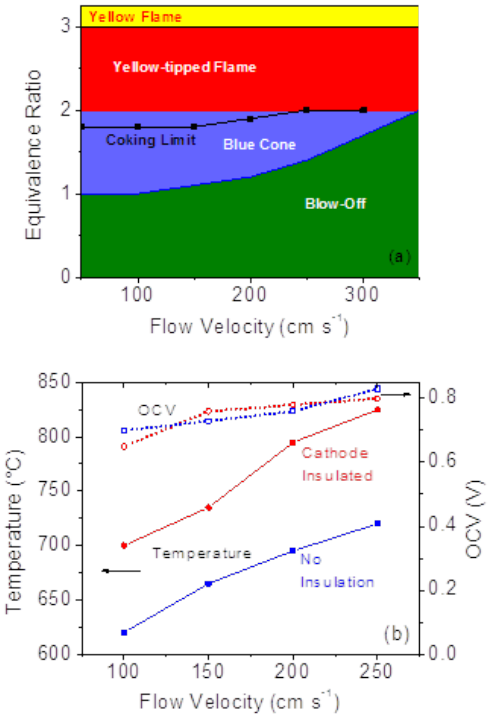

Figure 2. Operating space. (a) Flame stability and quality for various fuel-air mixing parameters. The black data markers indicate the upper limit for coke-free operation when the cell is placed in the flame. (b) OCV (open markers) and temperature (closed markers) at equivalence ratio of 1.6, with (red) and without (blue) insulation place on the cathode side of the cell.

3.1.2 Insulation and cell angle

Initially, a cell was placed in the flame to determine the range of temperature and open circuit voltage (OCV) that can be expected for this setup, as shown in Figure 2b. At each flow velocity, the burner-to-cell gap was optimized to achieve the highest OCV. OCV greater than 0.75 V was only achieved at high flow velocity. Temperature ranged from about 625 to 725°C, which is on the low end of the operating temperature range for MS-SOFCs [30]. Therefore, we placed alumina wool insulation on the cathode side of the cell, which increased cell temperature by 75 to 100°C. The insulation did not have a large effect on OCV or optimum burner-to-cell gap. The insulation also reduced temperature gradient across the thickness and diameter of the cell. At 1.5 equivalence ratio and 200 cm s^{-1} flow velocity, without insulation, the anode was 100°C hotter and the cathode perimeter was 78°C colder than the center of the cathode side. With insulation, the temperature differences reduced to 68 and 53°C, respectively. Based on these results, insulation was used on top of the cell for the rest of the experiments discussed below. Additional data with no insulation is available in the Supplementary Information.

To determine the impact of cell-to-flame orientation, a cell was operated at various angles with the burner mounted vertically. The cell was hottest and produced the most power in a horizontal orientation. When tilted at 45°, the peak power was reduced by 11% with insulation and by 29% without insulation. Therefore, we attempted to maintain a perfectly horizontal cell orientation throughout the remainder of the experiments. Cell performance is not expected to be very sensitive to small errors in cell position, however.

3.2 Mapping the operating space

3.2.1 Cell position

Based on previous direct flame SOFC work, we expect cell performance to be very sensitive to the cell position with respect to the flame zones [6,20,21]. Figure 3a shows the variation in performance as a function of burner-to-cell gap for “low”-flow (equivalence ratio 1.4 and 100 cm s^{-1}) and “high”-flow (equivalence ratio 1.8 and 250 cm s^{-1}) fuel conditions. For low flow, most of the fuel is completely

combusted before reaching the cell, so OCV and power density are very low compared to the high flow situation for which high concentrations of electrochemically-active species can be expected in the vicinity of the anode. Aside from this quantitative difference, the trends are independent of fuel quantity. At high burner-to-cell gap, the OCV is low because most of the fuel is completely combusted before reaching the cell. As the cell is lowered into the flame and the anode comes in contact with the inner fuel-rich flame cone, the fuel concentration and therefore OCV increases dramatically. If the cell is lowered further and the inner flame cone spreads across the anode surface of the cell, temperature is reduced because the inner cone is so much colder than the secondary combustion zone, as discussed above in Section 3.1.1. The shape of the temperature profile is consistent with previous reports [20]. Peak power density goes through a maximum where the cell is close to the top of the inner cone, with the active anode area partially exposed to the inner cone environment. Above this height, the power is constrained by low OCV; below this height it is constrained by low cell temperature. A much broader maximum in power density is observed for high fuel condition, making the performance less sensitive to small variations in cell location or fluctuations in fuel flow (which controls flame size). Combined with higher power density, this suggests high fuel conditions are desirable for any flame-to-power application.

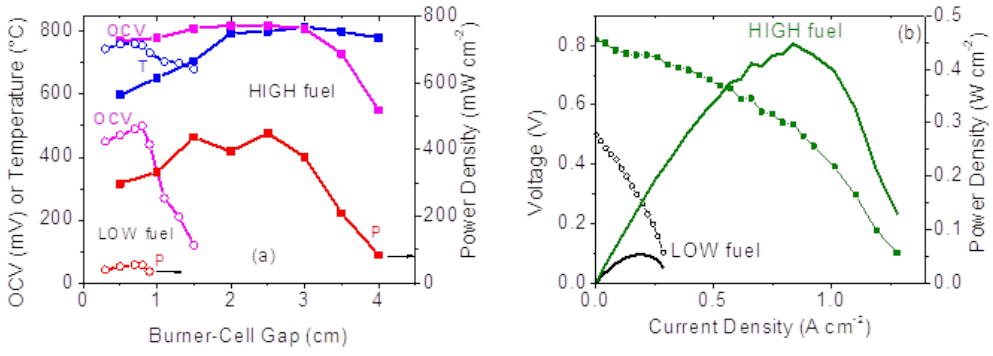

Figure 3. Impact of cell position and fuel-air flow. Cell was held at various burner-to-cell gap distances for both HIGH fuel flow (1.8 equivalence ratio, 250 cm s^{-1}, closed markers) and LOW fuel flow (1.4

equivalence ratio, 100 cm s^{-1}, open markers) conditions. (a) OCV (magenta), temperature (blue), and peak power density (red). (b) Polarization curves for HIGH fuel at 2.5 cm gap (green lines), and LOW fuel at 0.8 cm gap (black lines).

Polarization curves obtained at the optimum burner-to-cell gap for low and high fuel conditions are shown in Figure 3b. Although the cell temperature is only ~50°C higher for the high fuel case, the OCV and slope of the polarization curve are dramatically improved. In both cases, mass transport limitation is apparent at high current density. This is in contrast to the roughly linear polarization behavior observed for similar MS-SOFCs operating on pure hydrogen fuel [29]. These observations illustrate the importance of the flame conditions in terms of reforming the propane and delivering electrochemically-active fuel species to the anode, as opposed to simply providing heat to the cell.

3.2.2 Fuel-air mix and flow velocity

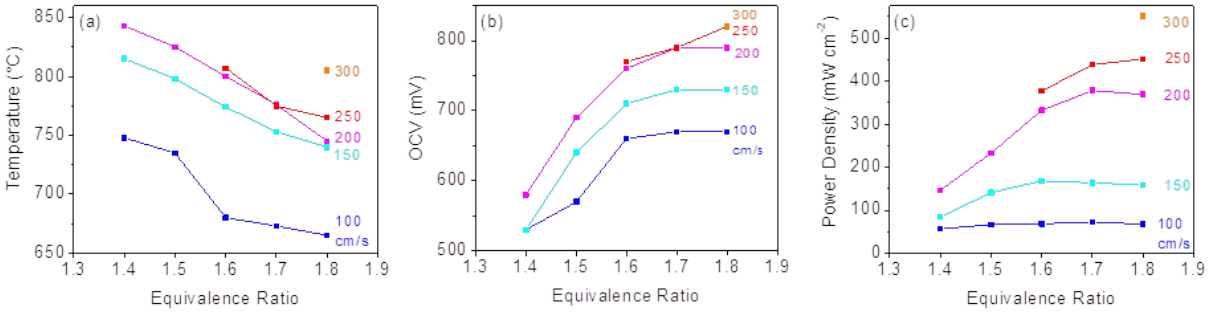

Figure 4. Impact of flame conditions on (a) temperature, (b) OCV, and (c) power density. Flow velocity is indicated by labels within the figures. Only combinations of equivalence ratio and flow velocity that lie within the area of interest defined in Figure 2a were studied.

Cell temperature and performance were mapped out over the operating space of interesting equivalence ratio and flow velocity, as shown in Figure 4. For each point, burner-to-cell gap was optimized to yield the highest peak power density achievable for each fuel condition. Temperature and OCV are quite sensitive to both fuel parameters. Higher flow velocity directly relates to higher fuel flowrate for a fixed equivalence ratio, providing more thermal output from the flame and therefore higher cell temperature, and larger fuel-rich area of the anode leading to higher OCV. For a fixed flow velocity, increasing the equivalence ratio reduces the oxygen available for primary combustion in the inner flame cone. This reduces the thermal output of the inner cone, reducing cell temperature, and increases the concentration of un-combusted and partially-combusted fuel species in the inner cone, increasing the OCV. Power density (Figure 4c) increases dramatically with flow velocity, as temperature and OCV work in concert. For a given flow velocity, power density is constrained by low OCV at low equivalence ratio, and by low temperature at high equivalence ratio. These trends are similar to those reported previously [6,18].

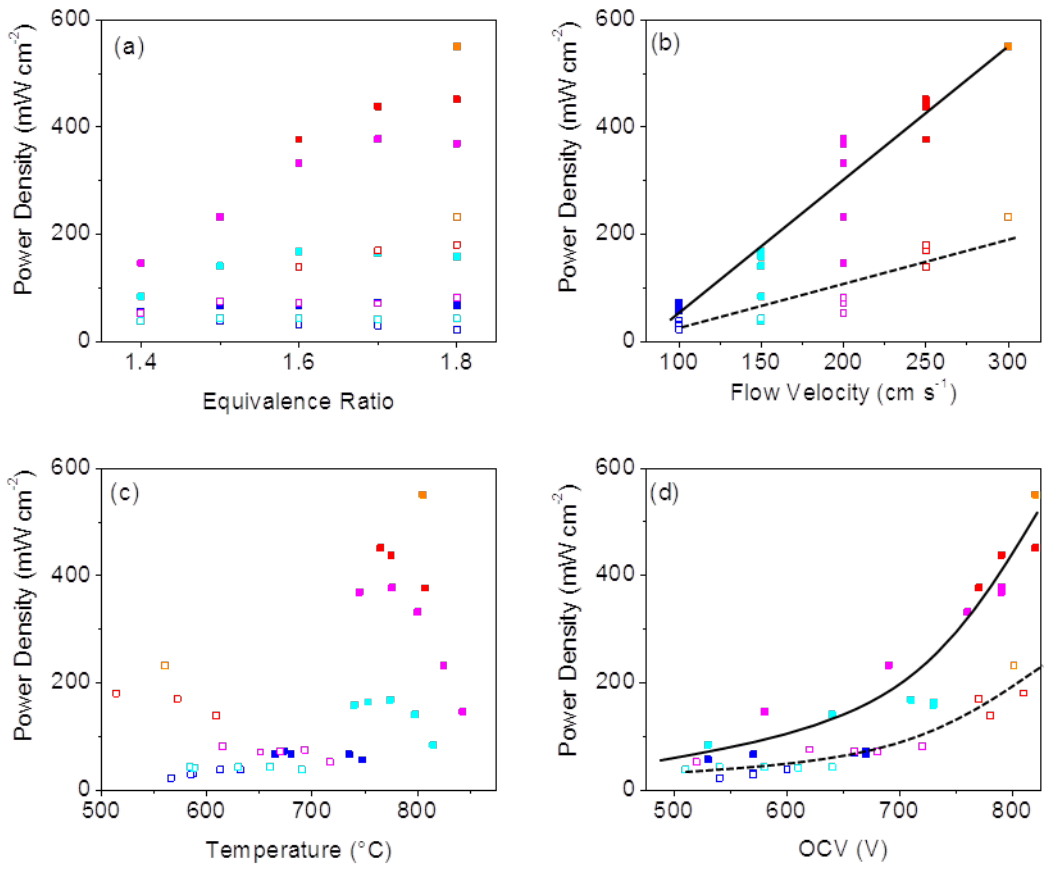

Figure 5. Correlation of power density to (a) equivalence ratio, (b) flow velocity, (c) temperature, and (d) OCV. The lines in (b) and (d) are guides for the eye. Cell operation with (closed markers, solid line) and without (open markers, dashed line) insulation on the cathode is displayed to show a wider range of operating points.

Figure 5 further elucidates which factors control cell performance. All power density data, including operation with no insulation taken from the Supplementary Information, is plotted as a function of equivalence ratio, flow velocity, temperature, and OCV to visualize the extent of correlation for each of these parameters. Performance is relatively uncorrelated with equivalence ratio and temperature. It

appears that flow velocity and OCV control the performance, underscoring the importance of electrochemically-active fuel species availability in the low-concentration environment of the flame.

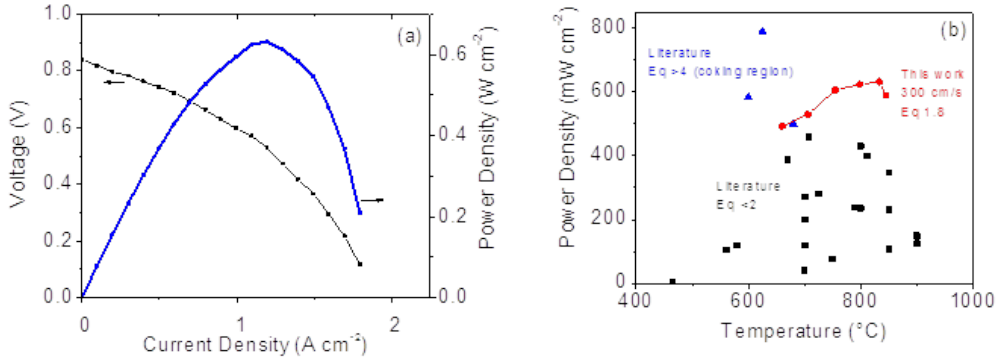

Figure 6. Optimal performance for a fresh MS-SOFC at 1.8 equivalence ratio and 300 cm s^{-1} flow velocity. (a) Polarization curve at 833°C. (b) Peak power obtained at a series of different burner-to-cell gaps (red circles) compared to highest peak power density reported in References [1-26] for equivalence ratio below 2 (black squares) or above 4 (blue triangles).

After determining that the highest power was achieved for flow velocity of 300 cm s^{-1} and equivalence ratio of 1.8 (Figure 4c), a fresh cell was tested under these conditions at various burner-to-cell gaps to access a variety of cell temperature. The highest performance achieved was 633 mW cm^{-2} at 833°C, as shown in Figure 6a. The results for various temperatures are summarized in Figure 6b, and compared to the highest performance shown in each of the available literature reports of direct-flame SOFC operation. The performance of the present MS-SOFCs is among the highest ever reported for direct-flame operation, and is exceeded only in cases where very high equivalence ratio was used (and where sooting and coking are expected during continuous operation). Almost all of the direct-flame reports in the literature use ASCs. In contrast, the MS-SOFCs used here contain anode supports with higher porosity and much larger pores (see Figure 1). The peak power achieved here in direct flame is roughly 60% of the 1.1 W cm^{-2} achieved at 700°C with pure hydrogen fuel by the same generation of MS-SOFCs, reported elsewhere

[29]. In contrast, a commercial ASC tested in direct-flame only achieved about 30% of the 0.83 W cm^{-2} achieved at 700°C with pure hydrogen fuel. Presumably, the open structure of these MS-SOFCs is an advantage for mass transport of electrochemically-active fuel species to the buried active anode layer and makes a large difference in the case of direct-flame operation, for which fuel species concentration is low.

3.3 Cell stability

3.3.1 Thermal Cycling

Upon placing the cell in contact with the flame, it heats up and becomes operational extremely quickly. As seen in Figure 7a, the cell reaches 600°C in about 20 s and the temperature stabilizes within one minute. This is one of the fastest startup times reported [9,12,18,20,21]. The initial heating rate is around 2000°C min^{-1}. The final OCV is achieved within 10 s, however, current generation is delayed by about 10 s and continues to increase until the cell is at the final operating temperature. The delay is this short even on the first cycle, during which the anode catalyst is reduced from the oxidized state maintained throughout catalyst infiltration. The rapid reduction can be attributed to the highly porous support and nano-scale NiO particles of the fresh MS-SOFC. This is in contrast to an ASC tested here that required several hours of flame impingement on the anode for full reduction to occur on the first cycle, consistent with similar ASC reduction timescale reported in the literature [12]. This is an important advantage of the MS-SOFC for black-start. The delay between OCV and current production is important to note, as some authors report the time to reach OCV as a "start-up" time metric, whereas the ability to produce useful power does not correspond to the OCV, but rather to the operating temperature [12,21].

Peak power density and OCV were recorded over 10 thermal cycles, and found to be quite stable as shown in Figure 7b. In particular, no evidence of cracking or delamination of the cell parts was observed. A similar cell used for demonstration purposes has undergone more than 100 flame-impingement heat-up cycles without any evident mechanical degradation.

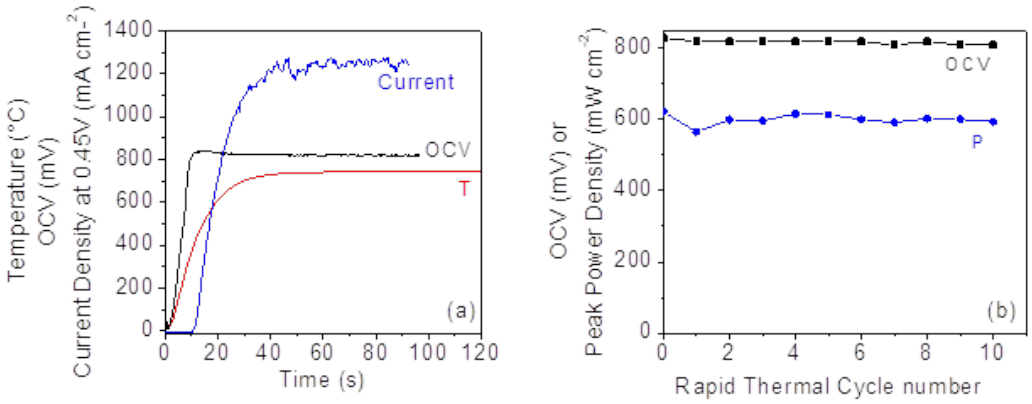

Figure 7. Rapid thermal cycling. (a) OCV (black), temperature (red), and current density at 0.45 V (blue) recorded upon placing the MS-SOFC into a flame operating at 1.7 equivalence ratio and 250 cm s^{-1} flow velocity. (b) OCV (squares) and peak power density (circles) after multiple thermal cycles. Burner-to-cell gap was maintained at 2 cm.

3.3.2 Continuous operation

A cell was operated semi-continuously at 0.45 V, chosen to correspond roughly to the peak power density (see Figure 6a). As seen in Figure 8, after an initial transient, the cell maintained stable operation over 20 h. Cell temperature was maintained at 765 to 785°C, except for the excursion at 10h when the propane tank ran empty and was replaced; cell performance recovered thereafter.

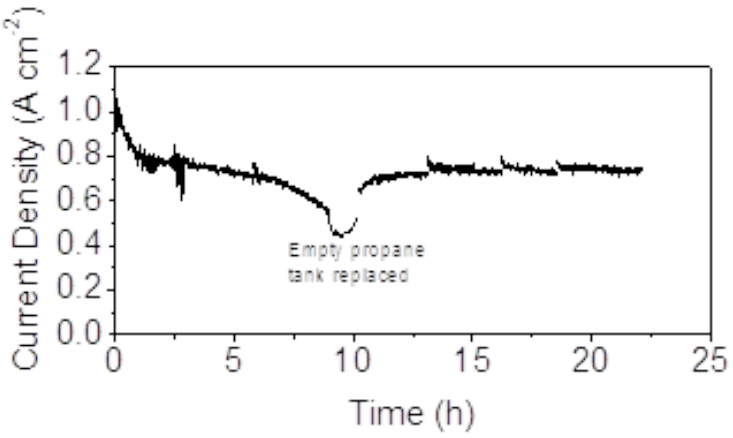

Figure 8. Continuous operation of MS-SOFC at 0.45 V in a flame operating at 1.7 equivalence ratio and 250 cm s-1 flow velocity. Burner-to-cell gap was maintained at 2 cm.

4. Summary

Symmetric-architecture metal-supported solid oxide fuel cells were fabricated with infiltrated catalysts on both anode and cathode side, and operated in direct-flame configuration. Various aspects of the flame and cell configuration were addressed to maximize performance. Performance was found to be quite sensitive to flow velocity and OCV. Performance was relatively uncorrelated to equivalence ratio or temperature. For an optimized cell and flame configuration, peak power density of 633 mW cm^{-2} at 833°C was achieved. This is among the highest power densities reported for direct-flame SOFCs to date. Extremely rapid startup is achieved within seconds of placing the cell in the flame, and the cell tolerates repeated rapid thermal cycling. Stable performance over >20 h of semi-continuous operation is achieved. The high performance, stable short-term operation, and tolerance to extremely rapid thermal cycling demonstrated for MS-SOFCs suggest they are well-suited for direct-flame applications.

Acknowledgements

The author acknowledges Grace Lau for assistance with sintering the cells used in this work. Funding for this work was provided by LBNL and the U.S. Department of Energy Office of Fossil Energy through a Technology Commercialization Fund grant number LBNL-17-TCF-16-12141. This work was funded in part by the U.S. Department of Energy under contract no. DE-AC02-05CH11231.

References

[1] J. Aguilar-Arias, D. Hotza, P. Lenormand, F. Ansart, Planar solid oxide fuel cells using PSZ, processed by sequential aqueous tape casting and constrained sintering, J. Am. Ceram. Soc. 96 (2013) 3075–3083. doi:10.1111/jace.12559.

[2] T. Hirasawa, S. Kato, A Study on Energy Conversion Efficiency of Direct Flame Fuel Cell Supported by Clustered Diffusion Microflames, J. Phys. Conf. Ser. 557 (2014) 12120. doi:10.1088/1742-6596/557/1/012120.

[3] M. Horiuchi, F. Katagiri, J. Yoshiike, S. Suganuma, Y. Tokutake, H. Kronemayer, W.G. Bessler, Performance of a solid oxide fuel cell couple operated via in situ catalytic partial oxidation of n-butane, J. Power Sources. 189 (2009) 950–957. doi:10.1016/j.jpowsour.2008.12.100.

[4] M. Horiuchi, S. Suganuma, M. Watanabe, Electrochemical Power Generation Directly from Combustion Flame of Gases, Liquids, and Solids, J. Electrochem. Soc. 151 (2004) A1402. doi:10.1149/1.1778168.

[5] M.M. Hossain, J. Myung, R. Lan, M. Cassidy, I. Burns, S. Tao, J.T.S. Irvine, Study on Direct Flame Solid Oxide Fuel Cell Using Flat Burner and Ethylene Flame, ECS Trans. 68 (2015) 1989–1999. doi:10.1149/06801.1989ecst.

[6] H. Kronemayer, D. Barzan, M. Horiuchi, S. Suganuma, Y. Tokutake, C. Schulz, W.G. Bessler, A direct-flame solid oxide fuel cell (DFFC) operated on methane, propane, and butane, J. Power Sources. 166 (2007) 120–126. doi:10.1016/j.jpowsour.2006.12.074.

[7] Y. Nakamura, S. Endo, Power generation performance of direct flame fuel cell (DFFC) impinged by small jet flames, J. Micromechanics Microengineering. 25 (2015) 104015. doi:10.1088/0960-1317/25/10/104015.

[8] L. Sun, Y. Hao, C. Zhang, R. Ran, Z. Shao, Coking-free direct-methanol-flame fuel cell with traditional nickel-cermet anode, Int. J. Hydrogen Energy. 35 (2010) 7971–7981. doi:10.1016/j.ijhydene.2010.05.048.

[9] Y. Tian, Z. Lü, B. Wei, Z. Wang, M. Liu, W. Li, X. Huang, W. Su, A non-sealed solid oxide fuel cell micro-stack with two gas channels, Int. J. Hydrogen Energy. 36 (2011) 7251–7256. doi:10.1016/j.ijhydene.2011.03.057.

[10] M. Vogler, D. Barzan, H. Kronemayer, C. Schulz, M. Horiuchi, S. Suganuma, Y. Tokutake, J. Warnatz, W.G. Bessler, Direct-Flame Solid-Oxide Fuel Cell (DFFC): A Thermally Self-Sustained, Air Self- Breathing, Hydrocarbon-Operated SOFC System in a Simple, No-Chamber Setup, ECS

Trans. 7 (2007) 555–564. doi:10.1149/1.2729136.

[11] Y. Wang, Y. Shi, X.K. Yu, N.S. Cai, S. Li, Direct Flame Fuel Cell Performance Using a Multi-element Diffusion Flame Burner, ECS Trans. 57 (2013) 279–288. doi:10.1017/CBO9781107415324.004.

[12] Y. Wang, Performance Characteristics of a Micro-tubular Solid Oxide Fuel Cell Operated with a Fuel-rich Methane Flame, ECS Trans. 68 (2015) 2237–2243. doi:10.1149/06801.2237ecst.

[13] Y. Wang, H. Zeng, T. Cao, Y. Shi, N. Cai, X. Ye, S. Wang, Start-up and operation characteristics of a flame fuel cell unit, Appl. Energy. 178 (2016) 415–421. doi:10.1016/j.apenergy.2016.06.067.

[14] Y. Wang, H. Zeng, Y. Shi, T. Cao, N. Cai, X. Ye, S. Wang, Power and heat co-generation by micro-tubular flame fuel cell on a porous media burner, Energy. 109 (2016) 117–123. doi:10.1016/j.energy.2016.04.095.

[15] K. Wang, R. Ran, Y. Hao, Z. Shao, W. Jin, N. Xu, A high-performance no-chamber fuel cell operated on ethanol flame, J. Power Sources. 177 (2008) 33–39. doi:10.1016/j.jpowsour.2007.11.004.

[16] Y.Q. Wang, Y.X. Shi, X.K. Yu, N.S. Cai, S.Q. Li, Integration of Solid Oxide Fuel Cells with Multi-Element Diffusion Flame Burners, J. Electrochem. Soc. 160 (2013) F1241–F1244. doi:10.1149/2.051311jes.

[17] Y. Wang, Y. Shi, X. Yu, N. Cai, J. Qian, S. Wang, Experimental Characterization of a Direct Methane Flame Solid Oxide Fuel Cell Power Generation Unit, J. Electrochem. Soc. 161 (2014) F1348–F1353. doi:10.1149/2.0381414jes.

[18] K. Wang, R.J. Milcarek, P. Zeng, J. Ahn, Flame-assisted fuel cells running methane, Int. J. Hydrogen Energy. 40 (2014) 4659–4665. doi:10.1016/j.ijhydene.2015.01.128.

[19] K. Wang, P. Zeng, J. Ahn, High performance direct flame fuel cell using a propane flame, Proc. Combust. Inst. 33 (2011) 3431–3437. doi:10.1016/j.proci.2010.07.047.

[20] Y. Wang, L. Sun, L. Luo, Y. Wu, L. Liu, J. Shi, The study of portable direct-flame solid oxide fuel cell (DF-SOFC) stack with butane fuel, J. Fuel Chem. Technol. 42 (2014) 1135–1139. doi:10.1016/S1872-5813(14)60045-1.

[21] X. Zhu, Z. Lü, B. Wei, X. Huang, Z. Wang, W. Su, Direct Flame SOFCs with La[sub 0.75]Sr[sub 0.25]Cr[sub 0.5]Mn[sub 0.5]O[sub 3−δ]⁄Ni Coimpregnated Yttria-Stabilized Zirconia Anodes Operated on Liquefied Petroleum Gas Flame, J. Electrochem. Soc. 157 (2010) B1838. doi:10.1149/1.3500976.

[22] X. Zhu, B. Wei, Z. Lü, L. Yang, X. Huang, Y. Zhang, M. Liu, A direct flame solid oxide fuel cell for potential combined heat and power generation, Int. J. Hydrogen Energy. 37 (2012) 8621–8629. doi:10.1016/j.ijhydene.2012.02.161.

[23] Y. Wang, Y. Shi, T. Cao, H. Zeng, N. Cai, X. Ye, S. Wang, A flame fuel cell stack powered by a porous media combustor, Int. J. Hydrogen Energy. (2017) 1–5. doi:10.1016/j.ijhydene.2017.01.088.

[24] R.J. Milcarek, M.J. Garrett, K. Wang, J. Ahn, Micro-tubular flame-assisted fuel cells running methane, Int. J. Hydrogen Energy. 41 (2016) 20670–20679. doi:10.1016/j.ijhydene.2016.08.155.

[25] R.J. Milcarek, M.J. Garrett, J. Ahn, Micro-tubular flame-assisted fuel cell stacks, Int. J. Hydrogen Energy. 41 (2016) 21489–21496. doi:10.1016/j.ijhydene.2016.09.005.

[26] R.J. Milcarek, K. Wang, R.L. Falkenstein-Smith, J. Ahn, Micro-tubular flame-assisted fuel cells for micro-combined heat and power systems, J. Power Sources. 306 (2016) 148–151. doi:10.1016/j.jpowsour.2015.12.018.

[27] Y. Wang, Y. Shi, M. Ni, N. Cai, A micro tri-generation system based on direct flame fuel cells for residential applications, Int. J. Hydrogen Energy. 39 (2014) 5996–6005. doi:10.1016/j.ijhydene.2014.01.183.

[28] M. Vogler, M. Horiuchi, W.G. Bessler, Modeling, simulation and optimization of a no-chamber solid oxide fuel cell operated with a flat-flame burner, J. Power Sources. 195 (2010) 7067–7077. doi:10.1016/j.jpowsour.2010.04.030.

[29] M.C. Tucker, Development of High Power Density Metal-Supported Solid Oxide Fuel Cells, Energy Technol. (2017).doi: 10.1002/ente.201700242

[30] M.C. Tucker, Progress in metal-supported solid oxide fuel cells: A review, J. Power Sources. 195 (2010) 4570–4582. doi:10.1016/j.jpowsour.2010.02.035.

[31] M.C. Tucker, G.Y. Lau, C.P. Jacobson, L.C. DeJonghe, S.J. Visco, Performance of metal-supported SOFCs with infiltrated electrodes, J. Power Sources. 171 (2007) 477–482. doi:10.1016/j.jpowsour.2007.06.076.

[32] T.Z. Sholklapper, V. Radmilovic, C.P. Jacobson, S.J. Visco, L.C. De Jonghe, Synthesis and Stability of a Nanoparticle-Infiltrated Solid Oxide Fuel Cell Electrode, Electrochem. Solid-State Lett. 10 (2007) B74–B76. doi:10.1149/1.2434203.

[33] C.K. Westbrook, F.L. Dryer, Simplified Reaction Mechanisms for the Oxidation of Hydrocarbon Fuels in Flames, Combust. Sci. Technol. 27 (1981) 31–43. doi:10.1080/00102208108946970.

[34] Ö.L. Gülder, Effects of oxygen on soot formation in methane, propane, and n-Butane diffusion flames, Combust. Flame. 101 (1995) 302–310. doi:10.1016/0010-2180(94)00217-G.

Figure Captions

Figure 1. MS-SOFC and flame setup. SEM image of (a,b) polished cross section of MS-SOFC structure after sintering and before catalyst infiltration, and (c) cathode pore after infiltration of LSM nanoparticles. Reproduced from Reference [29] with the permission of the publisher. Approximate layer thicknesses are: metal support 250 μm, porous electrode 20 μm, and electrolyte 10 μm. (d) Picture of the anode side of the

cell with flame impinging on the 1 cm^2 active area in the center of the cell. Alumina wool insulation is loosely placed on the cathode (top) side of the cell.

Figure 2. Operating space. (a) Flame stability and quality for various fuel-air mixing parameters. The black data markers indicate the upper limit for coke-free operation when the cell is placed in the flame. (b) OCV (open markers) and temperature (closed markers) at equivalence ratio of 1.6, with (red) and without (blue) insulation place on the cathode side of the cell.

Figure 3. Impact of cell position and fuel-air flow. Cell was held at various burner-to-cell gap distances for both HIGH fuel flow (1.8 equivalence ratio, 250 cm s^{-1}, closed markers) and LOW fuel flow (1.4 equivalence ratio, 100 cm s^{-1}, open markers) conditions. (a) OCV (magenta), temperature (blue), and peak power density (red). (b) Polarization curves for HIGH fuel at 2.5 cm gap (green lines), and LOW fuel at 0.8 cm gap (black lines).

Figure 4. Impact of flame conditions on (a) temperature, (b) OCV, and (c) power density. Flow velocity is indicated by labels within the figures. Only combinations of equivalence ratio and flow velocity that lie within the area of interest defined in Figure 2a were studied.

Figure 5. Correlation of power density to (a) equivalence ratio, (b) flow velocity, (c) temperature, and (d) OCV. The lines in (b) and (d) are guides for the eye. Cell operation with (closed markers, solid line) and without (open markers, dashed line) insulation on the cathode is displayed to show a wider range of operating points.

Figure 6. Optimal performance for a fresh MS-SOFC at 1.8 equivalence ratio and 300 cm s^{-1} flow velocity. (a) Polarization curve at 833°C. (b) Peak power obtained at a series of different burner-to-cell

gaps (red circles) compared to highest peak power density reported in References [1-26] for equivalence ratio below 2 (black squares) or above 4 (blue triangles).

Figure 7. Rapid thermal cycling. (a) OCV (black), temperature (red), and current density at 0.45 V (blue) recorded upon placing the MS-SOFC into a flame operating at 1.7 equivalence ratio and 250 cm s^{-1} flow velocity. (b) OCV (squares) and peak power density (circles) after multiple thermal cycles. Burner-to-cell gap was maintained at 2 cm.

Figure 8. Continuous operation of MS-SOFC at 0.45 V in a flame operating at 1.7 equivalence ratio and 250 cm s^{-1} flow velocity. Burner-to-cell gap was maintained at 2 cm.